Journal of Materials Chemistry A

PAPER

View Article Online
View Journal | View Issue

Cite this: J. Mater. Chem. A, 2018, 6, 1850

A Ga-doped SnO_2 mesoporous contact for UV stable highly efficient perovskite solar cells†

Bart Roose,[a] Christian M. Johansen,[a] Kevin Dupraz,[a] Thomas Jaouen,[b] Philipp Aebi,[b] Ullrich Steiner[a] and Antonio Abate*[ac]

Received 31st August 2017
Accepted 22nd December 2017

DOI: 10.1039/c7ta07663k

rsc.li/materials-a

Increasing the stability of perovskite solar cells is a major challenge for commercialization. The highest efficiencies so far have been achieved in perovskite solar cells employing mesoporous TiO_2 (m-TiO_2). One of the major causes of performance loss in these m-TiO_2-based perovskite solar cells is induced by UV-radiation. This UV instability can be solved by replacing TiO_2 with SnO_2; thus developing a mesoporous SnO_2 (m-SnO_2) perovskite solar cell is a promising approach to maximise efficiency and stability. However, the performance of mesoporous SnO_2 (m-SnO_2) perovskite solar cells has so far not been able to rival the performance of TiO_2 based perovskite solar cells. In this study, for the first time, high-efficiency m-SnO_2 perovskite solar cells are fabricated, by doping SnO_2 with gallium, yielding devices that can compete with TiO_2 based devices in terms of performance. We found that gallium doping severely decreases the trap state density in SnO_2, leading to a lower recombination rate. This, in turn, leads to an increased open circuit potential and fill factor, yielding a stabilised power conversion efficiency of 16.4%. The importance of high-efficiency m-SnO_2 based perovskite solar cells is underlined by stability data, showing a marked increase in stability under full solar spectrum illumination.

Introduction

Since the first report in 2009,[1] the power conversion efficiency (PCE) of perovskite solar cells (PSCs) has rapidly increased to more than 22%,[2] owing to the introduction of solid-state hole transporting materials[3,4] and optimised perovskite compositions[5–7] and deposition processes.[8–10] However, to make them commercially viable, the long-term stability of PSCs has to be greatly improved.[11–13] Reports so far have shown that a stability of up to 6 months can be achieved by optimising the perovskite composition,[7] the charge transporting layers[13–15] and the interface between perovskite and the charge transporting layers.[16] One of the major degradation pathways in PSCs involves a rapid decrease in performance upon UV-exposure.[14,17–19] This degradation is caused by both the desorption of oxygen from TiO_2, which exposes deep trap states and worsens the electronic properties of TiO_2 (ref. 14), and the photocatalytic properties of TiO_2, which degrade the organic components in the PSC.[19] To overcome these problems PSCs are typically tested in UV-free conditions.[11] This significantly reduces the impact of UV-induced degradation, but UV-filters do not block all UV-radiation (up to ~99.5%) and over a time span of 25 years UV-induced degradation may still play a significant role in performance loss. To make PSCs less susceptible to UV-induced degradation different electron transporting materials are being investigated.[20,21] SnO_2 is an especially promising candidate, owing to its large bandgap, making the material less sensitive to UV-radiation.[22] The performance of planar SnO_2 PSCs has rapidly come close to that of m-TiO_2 based PSCs, now achieving a PCE of 20.7%;[23] however, a mesoporous layer may further increase their performance by increasing electron extraction.[24] Also, planar SnO_2 based PSCs have been reported to be less stable than m-SnO_2 PSCs,[25,26] underlining the importance of highly efficient m-SnO_2 PSCs for UV-stable PSCs.

So far, the best-reported PCE of m-SnO_2 has been quite poor, with a stabilised PCE of 12.5% for high temperature processed m-SnO_2.[26] Higher PCEs have been reached employing low-temperature processed SnO_2 nanosheets (16.25% stabilized).[27,28] However, this structure is still very open and is midway between a planar and a truly mesoporous morphology and the resulting stability has not yet been investigated.

The relatively low PCE of m-SnO_2-based PSCs compared to m-TiO_2-based PSCs has two different causes, the first being the lower conduction band energy of SnO_2 compared to TiO_2.[22,29] Since the open circuit potential (V_{oc}) is influenced by the energy levels of the conduction band of the electron transporting material and the valence band of the hole transporting material, the lower conduction band energy of SnO_2 implies that the obtainable V_{oc} will be lower compared to TiO_2. Secondly, SnO_2-

[a]Adolphe Merkle Institute, Chemin des Verdiers 4, CH-1700 Fribourg, Switzerland
[b]Département de Physique, Fribourg Center for Nanomaterials, Université de Fribourg, CH-1700 Fribourg, Switzerland
[c]Helmholtz-Zentrum Berlin für Materialien und Energie, Kekuléstrasse 5, 12489 Berlin, Germany. E-mail: antonio.abate@helmholtz-berlin.de; antoniobate83@gmail.com

† Electronic supplementary information (ESI) available. See DOI: 10.1039/c7ta07663k

based PSCs tend to suffer from high recombination rates, further limiting the V_{oc} and fill factor (FF).[22] Doping of m-SnO_2 has been shown to be an effective way to increase device performance in dye-sensitized solar cells (DSSCs),[22] planar SnO_2 PSCs,[30,31] and nanosheet SnO_2 PSCs.[27] In DSSCs, gallium (Ga) was found to be one of the most promising dopants, showing impressive improvements in both V_{oc} and FF by reducing recombination.[32]

In this study, we address the high recombination rate of m-SnO_2 PSCs by Ga-doping. We show that Ga-doping greatly reduces the trap state density, leading to reduced recombination and as a result a large increase of V_{oc} and FF. As a result, we were able to achieve a stabilised PCE of 16.4%, rivalling the performance of m-TiO_2 PSCs made in our lab. In our previous work we found a significant increase in stability for m-SnO_2 based PSCs over m-TiO_2 based PSCs under maximum power point tracking conditions.[26] In addition, we show here that m-SnO_2 based PSCs are significantly more stable than m-TiO_2 based PSCs after 1000 hours of full solar spectrum illumination, underlining the superior UV-stability of m-SnO_2-based PSCs.

Results and discussion

Characterization of Ga-doped m-SnO_2

The inclusion of Ga was confirmed by X-ray photoelectron spectroscopy (XPS). The full XPS spectrum of Ga-doped SnO_2 can be found in ESI SI 1.† A close-up of the Ga $2p_{1/2}$ and Ga $2p_{3/2}$ is shown in Fig. 1a, clearly illustrating the presence of Ga. The Ga concentration was determined to be ~6%, higher than the amount of Ga in the precursor solution (2.5%). As XPS is a surface sensitive technique, only the top 1–2 nm of the sample is probed. This suggests that the Ga concentration is higher near the surface than in the bulk.

X-ray diffraction (XRD) was used to confirm the formation of rutile SnO_2. Fig. 1b shows the diffractograms of undoped and 2.5% Ga doped SnO_2; all peaks can be assigned to SnO_2, and no additional peaks are observed upon doping, indicating that Ga ions are incorporated into the SnO_2 lattice. Because Ga^{3+} has a slightly smaller ionic radius than Sn^{4+} (62 and 69 pm respectively[33]), the crystal lattice is expected to contract on the substitutional incorporation of Ga. This would result in an XRD peak shift to larger angles. Lattice parameters a and c can be determined using the formula for a tetragonal lattice;[34] a decreases upon doping from 4.721 Å to 4.706 Å and c decreases from 3.175 Å to 3.169 Å upon doping, indicating that Ga is incorporated into the SnO_2 lattice. The average crystallite size (D_c) can be calculated using the Scherrer equation.[35] D_c decreases from 15 ± 2 nm to 7 ± 1 nm upon doping. A reduced crystallite size is a frequently observed phenomenon in doping studies.[36]

Doping metal oxides can have large effects on the morphology of the electrode[34] and doping can thus affect the metal oxide–perovskite interface area and penetration of the perovskite into the mesoporous metal oxide network. To minimise the influence of morphology on device performance, the self-assembly of the amphiphilic *block*-copolymer polyisoprene-*block*-polyethylene oxide (PI-*b*-PEO) was used to direct the m-SnO_2 morphology.[18,37] Scanning electron microscope (SEM)

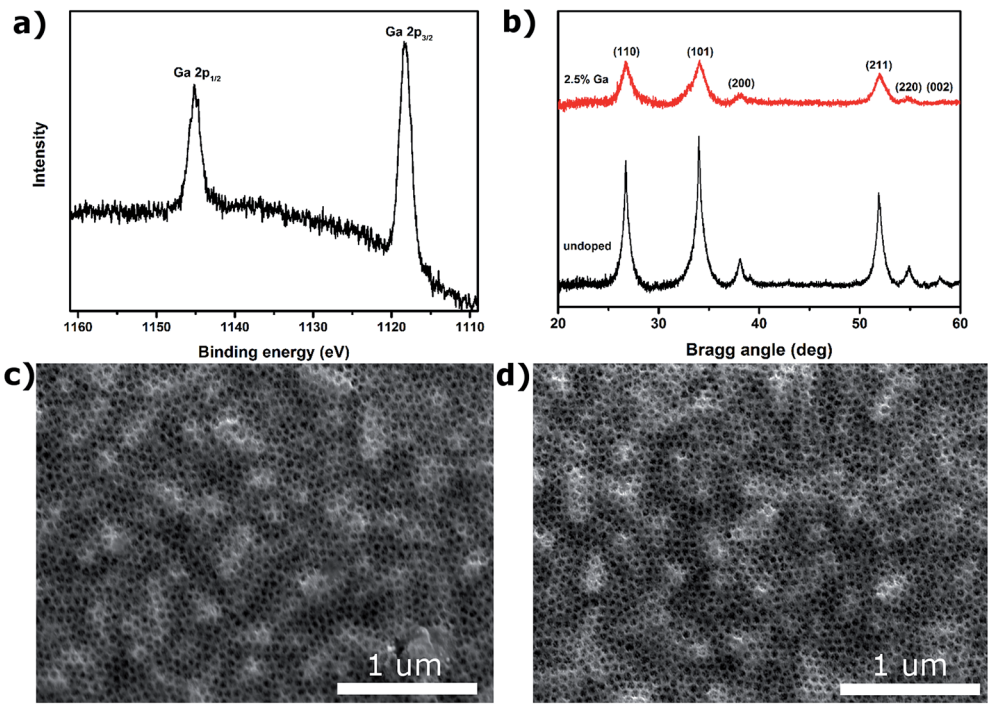

Fig. 1 (a) Close-up of the Ga $2p_{1/2}$ and Ga $2p_{2/3}$ XPS core level spectra. (b) XRD patterns of undoped and 2.5% Ga doped m-SnO_2. All peaks can be assigned to rutile SnO_2, and a slight contraction of the lattice is observed, indicating that Ga is incorporated into the SnO_2 lattice. (c) SEM micrographs of undoped m-SnO_2 and (d) 2.5% Ga-doped m-SnO_2, showing an identical morphology for undoped and doped samples.

micrographs showed mesoporous structures with similar pore sizes for undoped (54 ± 13 nm) and doped (57 ± 12) SnO_2 films (Fig. 1c and d). The similar pore size indicates that the morphology is not changed by doping and rules out any influence of morphology on device performance.

Photovoltaic performance

PSCs employing Ga-doped m-SnO_2 were fabricated according to the literature.[6,26] Teh *et al.* found an optimum Ga concentration of 3% for DSSCs;[32] it was thus decided to probe this parameter in the range between 1.5 and 3.5% and an optimal Ga-precursor concentration of 2.5% was found (ESI SI 2†). An excess of doping can lead to a decrease in device performance either by raising the conduction band so far that electron injection becomes inefficient, in which case V_{oc} keeps increasing, but J_{sc} decreases, or the dopant induces trap states, leading to a decrease of all device parameters. In this study, higher doping concentrations cause all photovoltaic parameters to decrease, indicating that at these concentrations doping induces the formation of trap states.[22,34] The SEM micrograph in Fig. 2a shows the cross-section of a photovoltaic device employing an ~100 nm thick layer of mesoporous SnO_2. The photocurrent–voltage (J–V) curves of the PSCs measured under AM1.5 simulated solar light (100 mW cm^{-2}) illumination are shown in Fig. 2b. The photovoltaic parameters extracted from the J–V curves, the open-circuit potential (V_{oc}), short-circuit current density (J_{sc}), fill factor (FF), power conversion efficiency (PCE) and the stabilised power output efficiency after 150 s, are shown in Table 1 (average of 7 devices). Because the obtained efficiency in PSCs is dependent on the way the device is measured (preconditioning bias light and voltage, scan speed and direction), it is necessary to determine efficiency by a method other than using the J–V curve. By determining the maximum power point and keeping the system at the corresponding voltage for extended periods of time, a PCE value can be determined that resembles the PCE of a device under real-world working conditions.[38] For completeness forward and backward scans were measured, and they can be found in ESI SI 3† (note that hysteresis is quite severe; this may be due to the reversal of the "light soaking" effect described by Tiwana *et al.*[39] under short circuit conditions). External quantum efficiency (EQE) spectra are shown in ESI SI 4;† the integrated J_{sc} is in good agreement with the value extracted from J–V curves.

PCE values show an increase of approximately 25% upon Ga-doping, which can be attributed to an increase in V_{oc} and FF, while J_{sc} remains unchanged. Note that the stabilized PCE is in some cases even higher than the PCE extracted from the J–V curve; this can be attributed to light soaking which has been reported to improve the properties of SnO_2 (ref. 39) and spiro-OMeTAD.[40] The PCE of Ga-doped m-SnO_2 based PSCs rivals that of m-TiO_2 based PSCs constructed in our lab (ESI SI 5†). To further investigate the origin of the increase in device performance we performed several (opto-) electronic measurements, including Mott–Schottky analysis of m-SnO_2 electrodes to investigate the conduction band energy and density of free charges, charge extraction measurements of complete PSCs to probe the trap state density and IMVS and IMPS of DSSCs (because of the overlapping signals of perovskite and the electron transporting material[41]) to find the electron transport lifetime and recombination rate.

Mott–Schottky analysis (Fig. 3a) was used to reveal changes in the conduction band energy. The flat band potential (V_{fb}) is the external voltage for which no band bending occurs and corresponds to the intersection of the linear part of the curve with the x-axis.[42] As the severity of the band bending depends on the conduction band position, a V_{fb} shift is indicative of the relative position of the conduction band. Fig. 3a shows that V_{fb} is slightly negatively shifted from −0.452 V to −0.458 V, corresponding to an increase of 6 mV of V_{oc} as a result of the conduction band shift. The observed ~70 mV increase of V_{oc} in the devices is much larger and may be attributed to reduced recombination. Because of the small conduction band shift, the electron injection efficiency from the perovskite absorber into SnO_2 is not expected to change and have an effect on J_{sc}.

The slope of the linear part of the curve in Fig. 3a can be used to deduce the number of free electrons (N_e) using eqn (1)

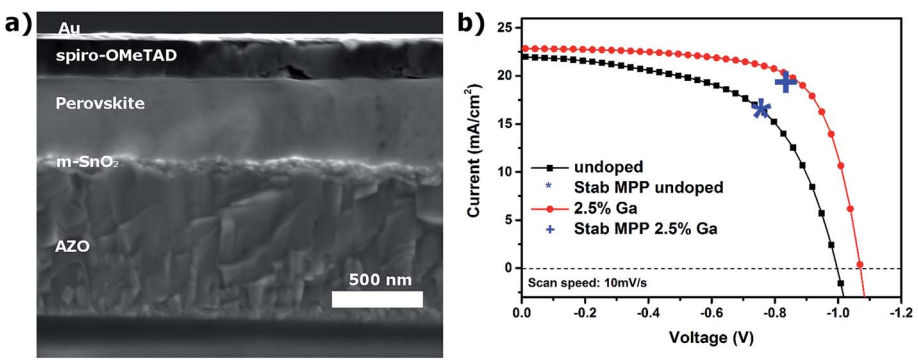

Fig. 2 (a) SEM cross-section of a photovoltaic device, consisting of an aluminium doped zinc oxide (AZO) transparent conductive electrode, compact SnO_2 ESL, 100 nm mesoporous SnO_2, perovskite capping layer, spiro-OMeTAD hole conducting layer and gold back contact. (b) J–V curves of PSCs employing undoped and 2.5% Ga-doped SnO_2. The stabilised maximum power point (Stab MPP) is indicated by an arrow. The J–V curves were measured from forward bias to short circuit conditions at a scan rate of 10 mV s^{-1} under AM1.5 simulated solar light (100 mW cm^{-2}) illumination. The cells were masked (0.09 cm^2) and characterised five days after their preparation.

Table 1 Photovoltaic parameters of Ga-doped SnO_2, average of 7 devices and best-performing devices: open-circuit voltage (V_{oc}), short-circuit current density (J_{sc}), fill factor (FF), power conversion efficiency (PCE) extracted from the J–V curves in Fig. 2 and stabilized power conversion efficiency (Stab. PCE) after 150 seconds. The J–V characteristics were recorded scanning from forward bias to short circuit conditions at a scan rate of 10 mV s^{-1} across a 0.09 cm^2 aperture active area. The voltage at the maximum power output was extracted from the J–V curves and the devices were then held at this voltage to determine the variation of the power output efficiency with time

Ga (%)	V_{oc} (mV)	(J_{sc} (mA cm^{-2})	FF (%)	PCE (%)	Stab. PCE (%)
0, average	988 ± 16	21.6 ± 0.3	57 ± 1	12.1 ± 0.3	12.2 ± 0.3
0, best	997	22.0	57	12.5	12.7
2.5, average	1061 ± 10	22.1 ± 0.4	69 ± 1	16.3 ± 0.3	15.8 ± 0.3
2.5, best	1070	22.8	70	17.0	16.4

$$\text{Slope} = \frac{2}{\varepsilon\varepsilon_0 A^2 e N_e} \quad (1)$$

where ε_0 is the permittivity of free space, ε the dielectric constant of the material, A the sample area and e the electronic charge. Upon doping, N_e increases from 2.5 × 10^{17} cm^{-2} to 6.0 × 10^{17} cm^{-2}; this will have an effect on J_{sc} as the conductivity (σ) of the metal oxide is given by eqn (2)

$$\sigma = N_e \mu_e \quad (2)$$

where μ_e is the mobility of the electrons. If the mobility is unchanged, an increase of N_e results in a higher conductivity and may have a positive effect on J_{sc}. Electron mobility can be measured using IMPS. The increase of N_e is somewhat unexpected, as Ga^{3+} is a p-type dopant if it were to replace Sn^{4+}. It is thus likely that some Ga^{3+} is incorporated interstitially, where it can donate electrons to increase N_e. The positive slope also indicates that both SnO_2 and Ga-doped SnO_2 are n-type.[42]

Charge extraction measurements were performed to quantify the trap state density of undoped and doped m-SnO_2 (Fig. 3b). The cell was operated under illumination at V_{oc}, after which the illumination was switched off, and the V_{oc} was allowed to decay for a set time, after which the cell was switched to short circuit, and the remaining charge was collected. The amount of charge left in the cell at a certain voltage is directly proportional to the number of energy states at this voltage.[13] Because these energy states are below the conduction band, they act as electron traps and have a detrimental effect on device performance by acting as recombination centres and slowing down charge transport. Fig. 3b illustrates the drastic reduction of trap states upon doping as much less charge is collected for a similar voltage. It is expected that as a result recombination is reduced and electron mobility increased.

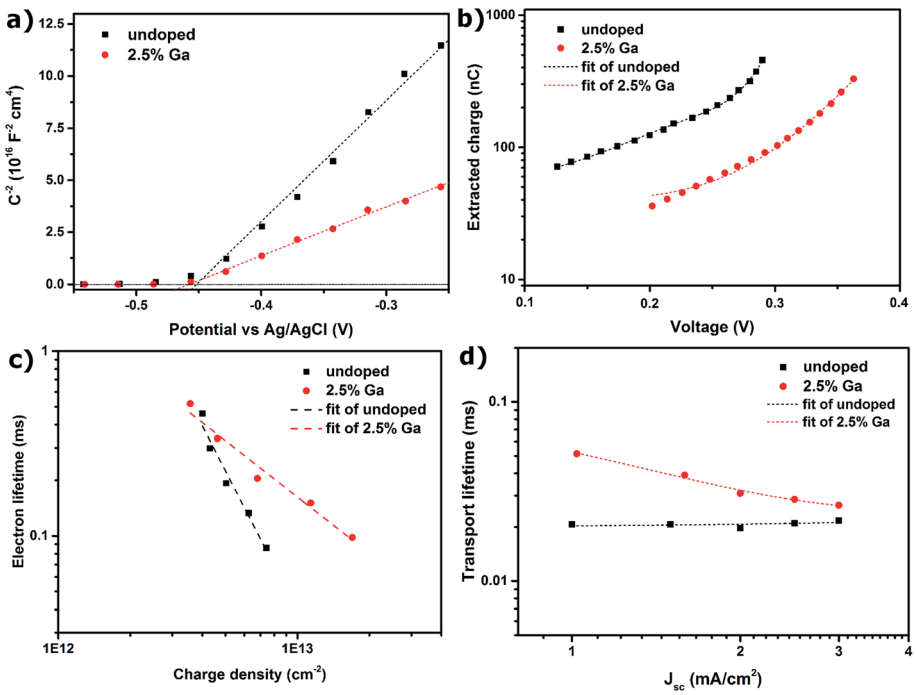

Fig. 3 Optoelectronic analysis of undoped and 2.5% Ga-doped m-SnO_2 devices: (a) Mott–Schottky plot; the electrodes were submerged in a 0.5 M KCl solution, with a Pt counter electrode and Ag/AgCl reference electrode, (b) charge extracted at open circuit as a function of the voltage, (c) electron lifetime for undoped and 2.5% Ga-doped m-SnO_2 in solid-state DSSCs, as a function of open circuit voltage (V_{oc}), obtained through IMVS, (d) electron transport lifetimes for undoped and 2.5% Ga-doped m-SnO_2 in solid-state DSSCs as a function of the short-circuit current density (J_{sc}), obtained through IMPS. IMPS and IMVS data are well fit by a single exponential.

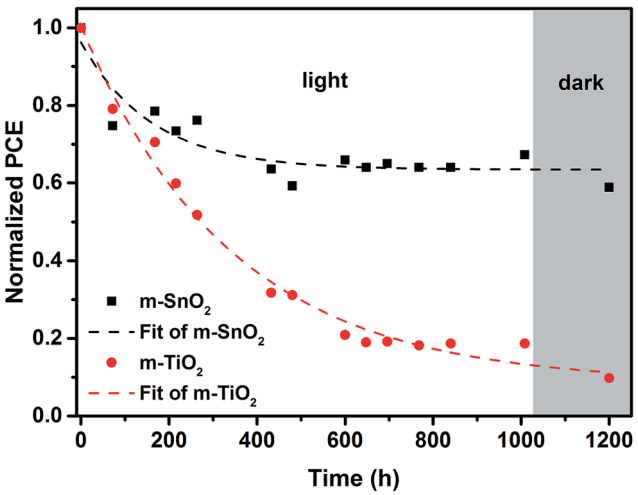

Fig. 4 Normalized PCE of m-SnO_2 and m-TiO_2 as a function of time under full spectrum illumination (100 mW cm^{-2}). The devices were placed in a glovebox with an N_2 atmosphere (~500 ppm O_2) during the illumination and were removed from the glovebox to extract the normalised PCE. After ~1000 hours of illumination, the devices were stored in the dark and measured again after 200 hours.

Because the observed increase in V_{oc} cannot be exclusively explained by a shift of the conduction band of SnO_2, IMVS was performed to determine the recombination lifetime (electron lifetime) of undoped and Ga-doped m-SnO_2 devices (Fig. 3c).[43] Because electron transport and recombination in metal oxides and perovskite have similar lifetimes,[41] DSSCs were used for intensity modulated photocurrent spectroscopy (IMPS) and IMVS measurements instead. Fig. 3c shows an order of magnitude lower recombination for Ga-doped m-SnO_2 based DSSCs, which is largely responsible for the observed increase of V_{oc}. Similarly, the decreased recombination rate results in reduced shunt resistance and an increase of FF. The decreased recombination rate is likely to be a result of the lower trap state density in Ga-doped m-SnO_2 devices. A second possibility may be the formation of a thin charge barrier layer at the surface of SnO_2, as XPS data showed a higher concentration of Ga near the surface. Such thin charge barrier layers have been reported to reduce recombination.[44] However, the difference in the slopes of the two curves is indicative of the absence of a barrier layer.[45]

The charge transport rate (transport lifetime) was determined by IMPS (Fig. 3d). Electron transport is faster for undoped devices at low current densities, which indicates a reduced mobility of the electrons after incorporation of Ga. This reduced mobility may be the result of a charge barrier layer at the surface of SnO_2.[44] However, the curves converge for higher current densities and electron transport rates will be very similar for current densities commonly achieved in PSCs (~20 mA cm^{-2}). This increased mobility of electrons in Ga-doped m-SnO_2 at higher current density is a result of the reduced deep trap state density compared to undoped m-SnO_2. As mobility is unchanged upon doping and the number of free electrons increases, the conductivity of Ga-doped SnO_2 is higher than that of undoped SnO_2 (eqn (2)), increasing J_{sc}.

The decreased number of trap states is likely to be the result of the elimination of oxygen vacancies in the SnO_2 lattice by incorporation of Ga^{3+} ions, similar to what has been reported for TiO_2, with the Ga^{3+} dopant replacing under-coordinated Sn ions, eliminating oxygen vacancies.[17]

For doping concentrations higher than 2.5% the PCE starts to decrease gradually. ESI SI 6† shows that this is due to an increasing trap state density caused by the Ga dopant, which results in shorter electron lifetimes (higher recombination) and longer transport lifetimes (reduced mobility).

Stability

The stability of state-of-the-art m-TiO_2 based PSCs[7] was compared to that of m-SnO_2 based PSCs. In our previous work we showed that m-SnO_2 based PSCs had superior stability under maximum power point tracking conditions, as compared to the commonly used m-TiO_2.[26] Fig. 4 shows that m-SnO_2 based PSCs are also more stable than m-TiO_2 based PSCs when the devices are subjected to 1000 hours of full spectrum illumination (100 mW cm^{-2}). Both m-SnO_2 and m-TiO_2 based PSCs show a rapid drop to 80% within the first 100 hours of testing. After this, the normalised PCE of m-SnO_2 based PSCs stabilises at around 70%

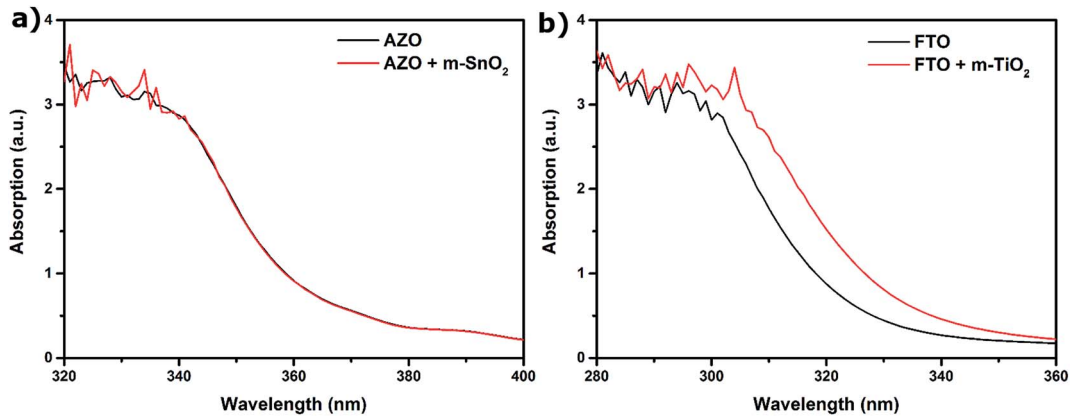

Fig. 5 UV/vis absorption spectra of (a) m-SnO_2 and (b) m-TiO_2, illustrating that m-SnO_2 absorbs no light in a device configuration, whereas m-TiO_2 does absorb a significant amount of light.

of the initial PCE up to 1000 hours of full spectrum illumination. The normalised PCE of m-TiO_2 based PSCs decreases much further and retains only 20% of the initial PCE after 1000 hours of full spectrum illumination. The degradation of PSCs has been ascribed to several different mechanisms related to the metal oxide component, the main ones being UV-light induced desorption of O_2 from the metal oxide surface[17,18] and the photocatalytic properties of TiO_2 actively degrading the perovskite light absorber.[19,34] After storing the devices in the dark for 200 hours, the PCE does not recover. As O_2 desorption is reversible, this process can be excluded, leaving the photocatalytic degradation catalyzed by the metal oxide as the most likely degradation pathway.

As TiO_2 has a smaller bandgap than SnO_2, it is more photocatalytically active under these conditions. Also, it was found that SnO_2 deposited on electrode coated glass absorbs no UV-light at all (Fig. 5a), making it inactive as a photocatalyst, whereas TiO_2 does absorb a substantial amount of UV-light (Fig. 5b). It has to be noted that m-SnO_2 based PSCs were deposited on AZO, as it was shown previously that fluorine migration from FTO to the SnO_2 compact layer could severely decrease device performance.[26] However, the same behavior is observed for m-SnO_2 deposited onto FTO and m-TiO_2 deposited onto AZO (ESI SI 7†) and the performance loss for m-TiO_2 based PSCs on AZO electrodes was found to be similar to that of their FTO counterparts (ESI SI 8†). The discrepancy in UV-activated photocatalytic behaviour can explain the observed difference in stability between m-SnO_2 and m-TiO_2 based PSCs.

Conclusions

We found that m-SnO_2-based devices suffer from high recombination rates, limiting V_{oc} and FF. Ga-doping eliminates deep trap states that act as recombination centres, leading to a marked increase in V_{oc} and FF. Ga-doped m-SnO_2 based PSCs were shown to reach a stabilised PCE of 16.4%, compared to 12.7% for undoped m-SnO_2 devices, presenting for the first time m-SnO_2-based PSCs that can compete with state-of-the-art m-TiO_2-based PSCs. Additionally, m-SnO_2 based PSCs proved to be more stable than m-TiO_2 based PSCs due to the larger bandgap of SnO_2, making SnO_2 less photocatalytically active than TiO_2. We have shown that it is possible to replace m-TiO_2, which has yielded the highest efficiency in PSCs so far, with a more stable alternative, without losing performance. This is an important step towards the commercialisation of PSCs.

Experimental

X-ray photoelectron spectroscopy

XPS measurements were performed with an upgraded OMICRON-SCIENTA DA30-R8000 analyser using a SPECS XR 50 Al Kα ($h\nu$ = 1486.7 eV) X-ray anode and a FOCUS 500 X-ray monochromator. All spectra were obtained at room temperature in transmission mode on the as-is sample surfaces. During the measurements, the pressure in the chamber did not exceed 2×10^{-10} mbar. The Ga doping concentration was estimated from the XPS measurements by calculating the cross-sectional weighted intensity ratio of the Sn $3d_{5/2}$ and Ga $2p_{3/2}$ core levels.

Scanning electron microscopy

Scanning electron microscopy was carried out on a Tescan MIRA 3 LMH with a field emission source operating at an acceleration voltage of 10 kV. Pore sizes were calculated using ImageJ.

X-ray diffraction

X-ray diffraction was measured using a Rigaku Ultima IV with a Cu Kα source ($\lambda = 0.154056$ nm) equipped with a dual position graphite diffracted beam monochromator and a scintillation counter detector, operating in Bragg–Brentano geometry. A step size of 0.01 deg was chosen and an acquisition time of 2 min deg^{-1} and a baseline correction were applied.

Solar cell preparation

Aluminum doped zinc oxide coated glass slides (Zhuhai Kaivo Optoelectronic Technology Co., <10 $\square^{-1}$) were cleaned by sonication in deionized water for 15 minutes. After rinsing with deionized water and ethanol, the substrates were again sonicated with isopropanol and rinsed with acetone. The substrates were treated with UV-ozone for 5 minutes, and a 30 nm thick SnO_2 ESL was deposited by spray pyrolysis at 450 °C from a precursor solution of butyltin trichloride (250 mM) in anhydrous ethanol.[46] Gallium(III) acetylacetonate (99.99%) was added to the precursor solution to reach the desired doping concentration. Mesostructured SnO_2 electrodes were synthesized using a structure directing *block*-copolymer.[37] A tin oxide precursor sol was prepared by dissolving poly(1,4-isoprene-*b*-ethylene oxide) (25 mg, polymer source, Mn: PIp(50000)-PEO(12000), M_w/M_n: 1.05) in tetrahydrofuran (1 ml), after which tin(IV) chloride pentahydrate (80 mg) and gallium(III) acetylacetonate were added and the mixture stirred for 30 minutes. The resulting solution was spin-coated (4000 rpm, 10 s) onto the substrate. The films were annealed on a programmable hotplate (2000 W, Harry Gestigkeit GmbH) using a 45 minute ramp to 450 °C followed by a dwell time of 30 minutes to remove the *block*-copolymer template and crystallise SnO_2. FTO coated glass slides (Sigma Aldrich, 10 $\square^{-1}$) were cleaned by sonication in a 2% Hellmanex aqueous solution for 30 min. After rinsing with deionized water and ethanol, the substrates were further cleaned by UV ozone treatment for 15 min. Then, a 30 nm TiO_2 compact layer was deposited on FTO *via* spray pyrolysis at 450 °C from a precursor solution of titanium diisopropoxide bis(acetylacetonate) in anhydrous ethanol. After the spraying, the substrates were treated at 450 °C for 45 min and left to cool down to room temperature. Then, a mesoporous TiO_2 layer was deposited by spin coating for 20 s at 4000 rpm with a ramp rate of 2000 rpm s^{-1}, using a 30 nm particle paste (Dyesol 30 NR-D) diluted in ethanol to achieve a 150–200 nm thick layer. After the spin coating, the substrates were dried at 100 °C for 10 min and then sintered again at 450 °C for 30 min under dry air flow. Li-doping of mesoporous TiO_2, as described elsewhere,[41] was accomplished by spin coating a 0.1 M solution

of Li-TFSI in acetonitrile at 3000 rpm for 10 s followed by another sintering step at 450 °C for 30 min. The perovskite and HTM were deposited according to the literature.[6,47] Perovskite films were deposited from a precursor solution containing FAI (1 M), PbI_2 (1.1 M), MABr (0.2 M), $PbBr_2$ (0.2 M) and CsI (0.075 M) in anhydrous DMF : DMSO 4 : 1 (v/v). The perovskite solution was spin-coated in a two-step program at 1000 and 6000 rpm for 10 and 20 s respectively. During the second step, 100 μl of chlorobenzene was poured onto the spinning substrate 5 seconds prior to the end of the program. The substrates were then annealed at 100 °C for 1 hour in a nitrogen-filled glovebox. Subsequently, the substrates were cooled down for a few minutes and a spiro-OMeTAD (Luminescence Technology) solution (70 mM in chlorobenzene) doped with bis(trifluoromethylsulfonyl)imide lithium salt (Li-TFSI, Aldrich), tris(2-(1*H*-pyrazol-1-yl)-4-*tert*-butylpyridine)–cobalt(III)tris(bis(trifluorouoromethylsulfonyl)imide) (FK209, Dyenamo) and 4-*tert*-butylpyridine (TBP, Aldrich) was spun at 4000 rpm for 20 s. The molar ratios of additives for spiro-OMeTAD were 0.5, 0.03 and 3.3 for Li-TFSI, FK209 and TBP, respectively. Finally, 60 nm of gold was thermally evaporated under high vacuum on top of the device. Dye-sensitized solar cells were fabricated by employing Z907-dye as the light absorber instead of perovskite.[46]

Optoelectronic measurements

For photovoltaic measurements, a solar simulator from ABET Technologies (Model 11016 Sun 2000) with a xenon arc lamp was used, and the solar cell response was recorded using a Metrohm PGSTAT302N Autolab. The intensity of the solar simulator was calibrated to 100 mW cm^{-2} using a silicon reference cell from ReRa Solutions (KG5 filtered). *J–V* curves were measured in reverse bias (from high to low voltages), at a scan rate of 10 mV s^{-1}. For dark currents, a scan rate of 25 mV s^{-1} was used. The active area of the cells was 0.09 cm^2 and the cells were measured five days after their preparation. IMPS, IMVS and charge extraction measurements were performed according to a procedure described in the literature, using a white light LED driver at different light intensities and a Metrohm PGSTAT302N Autolab.[41,43]

Stability measurements

A solar simulator from ABET Technologies (Model 11016 Sun 2000) with a xenon arc lamp was used to illuminate the devices in an N_2-filled glovebox (containing ~500 ppm O_2). The intensity of the solar simulator was calibrated to 100 mW cm^{-2} using a silicon reference cell from ReRa Solutions (KG5 filtered). Devices were removed from the glovebox at set intervals to collect *J–V* curves as described above.

Mott–Schottky analysis

Flatband potentials and carrier densities were determined from Mott–Schottky plots, using an electrochemical method.[42] SnO_2 covered AZO substrates were submerged in a 0.5 M KCl solution, with a Pt counter electrode and Ag/AgCl reference electrode. The solution was purged with nitrogen before and during the measurements. The measurements were performed at a fixed frequency of 1 kHz at voltages ranging from −0.75 to −0.25 V.

Conflicts of interest

There are no conflicts of interest to declare.

Acknowledgements

The authors would like to acknowledge the Adolphe Merkle Foundation and the Swiss National Science Foundation (Program NRP70 No. 153990).

References

1 A. Kojima, K. Teshima, Y. Shirai and T. Miyasaka, *J. Am. Chem. Soc.*, 2009, **131**, 6050.
2 https://www.nrel.gov/pv/assets/images/efficiency-chart.png, accessed Sept. 2017.
3 H.-S. Kim, C.-R. Lee, J.-H. Im, K.-B. Lee, T. Moehl, A. Marchioro, S.-J. Moon, R. Humphry-Baker, J.-H. Yum, J. E. Moser, M. Graetzel and N.-G. Park, *Sci. Rep.*, 2012, **2**, 591.
4 M. M. Lee, J. Teuscher, T. Miyasaka, T. N. Murakami and H. J. Snaith, *Science*, 2012, **338**, 643.
5 N. J. Jeon, J. H. Noh, W. S. Yang, Y. C. Kim, S. Ryu, J. Seo and S. I. Seok, *Nature*, 2015, **517**, 476.
6 M. Saliba, T. Matsui, J.-Y. Seo, K. Domanski, J.-P. Correa-Baena, M. K. Nazeeruddin, S. M. Zakeeruddin, W. Tress, A. Abate, A. Hagfeldt and M. Graetzel, *Energy Environ. Sci.*, 2016, **9**, 1989.
7 M. Saliba, T. Matsui, K. Domanski, J.-S. Seo, A. Ummadisingu, S. M. Zakeeruddin, J.-P. Correa-Baena, W. R. Tress, A. Abate, A. Hagfeldt and M. Graetzel, *Science*, 2016, **354**, 206.
8 N. J. Jeon, J. H. Noh, Y. C. Kim, W. S. Yang, S. Ryu and S. I. Seok, *Nat. Mater.*, 2014, **13**, 897.
9 M. Liu, M. B. Johnston and H. J. Snaith, *Nature*, 2013, **501**, 395.
10 J. Burschka, N. Pellet, S.-J. Moon, R. Humphry-Baker, P. Gao, M. K. Nazeeruddin and M. Graetzel, *Nature*, 2013, **499**, 316.
11 F. Bella, G. Griffini, J.-P. Correa-Baena, G. Saracco, M. Graetzel, A. Hagfeldt, S. Turri and C. Gerbaldi, *Science*, 2016, **354**, 203.
12 K. Domanski, J.-P. Correa-Baena, N. Mine, M. K. Nazeeruddin, A. Abate, M. Saliba, W. Tress, A. Hagfeldt and M. Graetzel, *ACS Nano*, 2016, **10**, 6306.
13 A. Abate, S. Paek, F. Giordano, J.-P. Correa Baena, M. Saliba, P. Gao, T. Matsui, J. Ko, S. M. Zakeeruddin, K. H. Dahmen, A. Hagfeldt, M. Graetzel and M. K. Nazeeruddin, *Energy Environ. Sci.*, 2015, **8**, 2946.
14 T. Leijtens, G. E. Eperon, S. Pathak, A. Abate, M. M. Lee and H. J. Snaith, *Nat. Commun.*, 2013, **4**, 2885.
15 Y. Bai, Q. Dong, Y. Shao, Y. Deng, Q. Wang, L. Shen, D. Wang, W. Wei and J. Huang, *Nat. Commun.*, 2016, **7**, 12806.

16 H. Tan, A. Jain, O. Voznyy, X. Lan, F. P. García de Arquer, J. Z. Fan, R. Quintero-Bermudez, M. Yuan, B. Zhang, Y. Zhao, F. Fan, P. Li, L. N. Quan, Y. Zhao, Z.-H. Lu, Z. Yang, S. Hoogland and E. H. Sargent, *Science*, 2017, **355**, 722.
17 S. K. Pathak, A. Abate, P. Ruckdeschel, B. Roose, K. C. Gödel, Y. Vaynzof, A. Santhala, S.-I. Watanabe, D. J. Hollman, N. Noel, A. Sepe, U. Wiesner, R. Friend, H. J. Snaith and U. Steiner, *Adv. Funct. Mater.*, 2014, **24**, 6046.
18 B. Roose, K. C. Gödel, S. Pathak, A. Sadhanala, J. P. C. Baena, B. D. Wilts, H. J. Snaith, U. Wiesner, M. Graetzel, U. Steiner and A. Abate, *Adv. Energy Mater.*, 2016, **6**, 1501868.
19 S. Ito, S. Tanaka, K. Manabe and H. Nishino, *J. Phys. Chem. C*, 2014, **118**, 16995.
20 J. You, L. Meng, T.-B. Song, T.-F. Guo, Y. Yang, W.-H. Chang, Z. Hong, H. Chen, H. Zhou, Q. Chen, Y. Liu and N. De Marco, *Nat. Nanotechnol.*, 2016, **11**, 75.
21 W. Chen, Y. Wu, Y. Yue, J. Liu, W. Zhang, X. Yang, H. Chen, E. Bi, I. Ashraful, M. Graetzel and L. Han, *Science*, 2015, **350**, 944.
22 Q. Wali, A. Fakharuddin and R. Jose, *J. Power Sources*, 2015, **293**, 1039.
23 E. H. Anaraki, A. Kermanpur, L. Steier, K. Domanski, T. Matsui, W. Tress, M. Saliba, A. Abate, M. Graetzel, A. Hagfeldt and J.-P. Correa-Baena, *Energy Environ. Sci.*, 2016, **9**, 3128.
24 E. Edri, S. Kirmayer, A. Henning, S. Mukhopadhyay, K. Gartsman, Y. Rosenwaks, G. Hodes and D. Cahen, *Nano Lett.*, 2014, **14**, 1000.
25 A. Fakharuddin, F. Di Giacomo, I. Ahmed, Q. Wali, T. M. Brown and R. Jose, *J. Power Sources*, 2015, **283**, 61.
26 B. Roose, J.-P. C. Baena, K. C. Gödel, M. Graetzel, A. Hagfeldt, U. Steiner and A. Abate, *Nano Energy*, 2016, **30**, 517.
27 G. Yang, H. Lei, H. Tao, X. Zheng, J. Ma, Q. Liu, W. Ke, Z. Chen, L. Xiong, P. Qin, Z. Chen, M. Qin, X. Lu, Y. Yan and G. Fang, *Small*, 2017, **13**, 1601769.
28 Q. Liu, M.-C. Qin, W.-J. Ke, X.-L. Zheng, Z. Chen, P.-L. Qin, L.-B. Xiong, H.-W. Lei, J.-W. Wan, J. Wen, G. Yang, J.-J. Ma, Z.-Y. Zhang and G.-J. Fang, *Adv. Funct. Mater.*, 2016, **26**, 6069.
29 J. P. Correa Baena, L. Steier, W. Tress, M. Saliba, S. Neutzner, T. Matsui, F. Giordano, T. J. Jacobsson, A. R. Srimath Kandada, S. M. Zakeeruddin, A. Petrozza, A. Abate, M. K. Nazeeruddin, M. Graetzel and A. Hagfeldt, *Energy Environ. Sci.*, 2015, **8**, 2928.
30 Y. Bai, Y. Fang, Y. Deng, Q. Wang, J. Zhao, X. Zheng, Y. Zhang and J. Huang, *ChemSusChem*, 2016, **9**, 2686.
31 M. Park, J.-Y. Kim, H. J. Son, C.-H. Lee, S. S. Jang and M. J. Ko, *Nano Energy*, 2016, **26**, 208.
32 J. J. Teh, S. L. Ting, K. C. Leong, J. Li and P. Chen, *ACS Appl. Mater. Interfaces*, 2013, **5**, 11377.
33 R. Shannon, *Acta Crystallogr.*, 1976, **32**, 751.
34 B. Roose, S. Pathak and U. Steiner, *Chem. Soc. Rev.*, 2015, **44**, 8326.
35 A. Patterson, *Phys. Rev.*, 1939, **56**, 978.
36 C. J. Brinker and G. W. Scherer, in *Sol-gel Science, the Physics and Chemistry of Sol-gel Processing*, Academic Press, Boston, 1990, ch. 4.
37 S. Guldin, P. Docampo, M. Stefik, G. Kamita, U. Wiesner, H. J. Snaith and U. Steiner, *Small*, 2012, **8**, 432.
38 H. J. Snaith, A. Abate, J. M. Ball, G. E. Eperon, T. Leijtens, N. K. Noel, S. D. Stranks, J. T.-W. Wang, K. Wojciechowski and W. Zhang, *J. Phys. Chem. Lett.*, 2014, **5**, 1511.
39 P. Tiwana, P. Docampo, M. B. Johnston, L. M. Herz and H. J. Snaith, *Energy Environ. Sci.*, 2012, **5**, 9566.
40 A. Abate, T. Leijtens, S. Pathak, J. Teuscher, R. Avolio, M. E. Errico, J. Kirkpatrik, J. M. Ball, P. Docampo, I. McPherson and H. J. Snaith, *Phys. Chem. Chem. Phys.*, 2013, **15**, 2572.
41 F. Giordano, A. Abate, J. P. Correa Baena, M. Saliba, T. Matsui, S. H. Im, S. M. Zakeeruddin, M. K. Nazeeruddin, A. Hagfeldt and M. Graetzel, *Nat. Commun.*, 2016, **7**, 10379.
42 K. Gelderman, L. Lee and S. W. Donne, *J. Chem. Educ.*, 2007, **84**, 685.
43 P. R. F. Barnes, K. Miettunen, X. Li, A. Y. Anderson, T. Bessho, M. Graetzel and B. C. O'Regan, *Adv. Mater.*, 2013, **25**, 1881.
44 A. K. Chandiran, M. K. Nazeeruddin and M. Graetzel, *Adv. Funct. Mater.*, 2014, **24**, 1615.
45 P. Docampo, P. Tiwana, N. Sakai, H. Miura, L. Herz, T. Murakami and H. J. Snaith, *J. Phys. Chem. C*, 2012, **116**, 22840.
46 P. Tiwana, P. Docampo, M. B. Johnston, H. J. Snaith and L. M. Herz, *ACS Nano*, 2011, **5**, 5158.
47 A. Abate, D. R. Staff, D. J. Hollman, H. J. Snaith and A. B. Walker, *Phys. Chem. Chem. Phys.*, 2014, **16**, 1132.